Shallow bore-hole three-axial fiber Bragg grating strain sensor for Etna volcano monitoring

E. Maccioni 🆔, U. Giacomelli 🆔, D. Carbone 🆔, S. Gambino 🆔, M. Orazi 🆔, R. Peluso 🆔, and F. Sorrentino 🆔

🌐 View Online   ⬆ Export Citation   🔴 CrossMark

ARTICLES YOU MAY BE INTERESTED IN

A variable-temperature scanning tunneling microscope operated in a continuous flow cryostat
Review of Scientific Instruments **90**, 093702 (2019); https://doi.org/10.1063/1.5118676

Transparent high-pressure nozzles for visualization of nozzle internal and external flow phenomena
Review of Scientific Instruments **90**, 033702 (2019); https://doi.org/10.1063/1.5065658

New light trap design for stray light reduction for a polarized scanning nephelometer
Review of Scientific Instruments **90**, 035113 (2019); https://doi.org/10.1063/1.5055672

Shallow bore-hole three-axial fiber Bragg grating strain sensor for Etna volcano monitoring

View Online   Export Citation   CrossMark

E. Maccioni,[1] [iD] U. Giacomelli,[1,a)] [iD] D. Carbone,[2] [iD] S. Gambino,[2] [iD] M. Orazi,[3] [iD] R. Peluso,[3] [iD] and F. Sorrentino[4] [iD]

AFFILIATIONS

[1] Dipartimento di Fisica "E. Fermi" - Università di Pisa, Largo B. Pontecorvo 3, 56127 Pisa, Italy

[2] Istituto Nazionale di Geofisica e Vulcanologia, Osservatorio Etneo, Piazza Roma 2, 95123 Catania, Italy

[3] Istituto Nazionale di Geofisica e Vulcanologia, Osservatorio Vesuviano, Via Diocleziano 328, 80124 Napoli, Italy

[4] Istituto Nazionale di Fisica Nucleare Sez. Genova, Via Dodecaneso 33, 16146 Genova, Italy and Marwan Technology, Largo B. Pontecorvo 3, 56127 Pisa, Italy

a) umberto.giacomelli@df.unipi.it

ABSTRACT

We present the realization, installation, and first results of a three-axial Fiber Bragg Grating (FBG) strain sensor prototype. This sensor has been developed in the framework of the Mediterranean supersite volcanoes (http://www.med-suv.eu, 2013) project and, in particular, with the aim at contributing to the study and monitoring of Etna volcano. The FBG sensor was installed in the facilities of the Serra La Nave Astrophysical Observatory (Catania, Italy) about 7 km south-west from the summit craters, at an elevation of about 1740 m. The three-axial device showed a dynamic range of some hundreds of microstrains with microstrain resolution (submicrostrain concerning the vertical component). That is a good trade-off among performances, cost, and power consumption. The sensor structure and its read-out system are innovative in their assembly and offers practical advantages in comparison with traditional strain meters. As a demonstration of the performances of our device, the data of about 28 months of operation are presented together with the records of some local, regional, and teleseismic events. The sensor along the vertical axis showed to be the best performing one, having a power spectral density of about -90 dB re. $1\varepsilon^2$/Hz around one day period.

Published under license by AIP Publishing. https://doi.org/10.1063/1.5086516

I. INTRODUCTION

Fiber optic and fiber Bragg grating (FBG) sensors have attained a large diffusion in the last years as cost-effective monitoring and diagnostic devices in civil engineering.[1,2] These sensors turned out to have an important impact in geophysics,[3,4] even if not so many submicrostrain performances are reported.[5,6] In order to monitor earthquakes and volcanoes, the measurement of crustal deformation through strain sensors is of crucial importance. Stress and strain behavior at volcanic areas is among the best indicators of changes in the activity of these systems. Conventional methods rely on the use of extensometers, dilatometers, and interferometers installed underground, but such sensors are large in size and need expensive and time-consuming installation procedures. An example of such instrumentation is given by deep bore-hole dilatometers and strainmeters that have been employed to monitor tectonic and volcanic activity.[7,8] However, these instruments, even though very sensitive and reliable, are expensive and require a large effort in preparing the site of installation. Fiber optic based devices offer low cost, small size, wide frequency band, easier deployment, and even the possibility of creating a local network with several sensors linked in an array.

A fiber Bragg grating is a periodical variation of the refractive index generated in the core of an optical fiber. It is typically obtained through UV radiation exposure with the help of a silica phase-mask having a suitable spatial windowing[9] which allows the determination of the spectral characteristics of the grating. When the radiation coming from a broadband light source (spectral width of some tens of nanometers) is injected into the fiber and interacts with the grating, only the wavelength in a narrow band (of the order of 0.2 nm) is reflected. The reflection wavelength is determined by the spacing of the individual grating planes, which is chosen during the manufacture of the Bragg grating itself. The reflected wavelength

is a function of the effective refractive index n_{eff} and of the grating period Λ,[10]

$$\lambda_b = 2 n_{eff} \Lambda. \tag{1}$$

For a single transmission mode fiber of given refractive index and core-cladding characteristics, the grating reflectivity $R(l, \lambda)$ is a function of the grating length l and wavelength λ. Any change in fiber properties, such as strain, temperature, or birefringence, which varies the modal index or grating pitch, will change the Bragg wavelength. The grating is an intrinsic sensor which changes the spectrum of an incident signal. If the strain ε (defined as the length gauge variation over its length) is homogeneous and isotropic, then

$$\frac{\delta \lambda_b}{\lambda_b} = (1 - p_e)\varepsilon \simeq 0.78\varepsilon, \tag{2}$$

where $p_e \simeq 0.21$ is the photo-elastic coefficient of silica fibers.[10] The typical value for the sensitivity to an applied axial strain is 1.2 picometer/microstrain ($pm/\mu\varepsilon$) at the wavelength of 1550 nm. The strain response is linear with no evidence of hysteresis up to some millistrain. The temperature sensitivity of a bare fiber FBG sensor is primarily due to the thermo-optic effect. It is given by

$$\frac{\delta \lambda_b}{\lambda_b} = \left(\alpha + \frac{1}{n} \frac{dn}{dT} \right) \Delta T, \tag{3}$$

with α being the silica thermal expansion coefficient, n being the refractive index, and T being the temperature. A typical value for the thermal response of a bare Bragg grating at 1550 nm inscribed in a Ge-doped silica fiber is 13.7 pm/°C.[10] When a load is applied to a structure containing the FBG sensor, the grating is strained causing a variation of the reflected Bragg wavelength, which in turn can be detected by means of a suitable read-out system. The main drawback is the simultaneous temperature dependence of the Bragg wavelength. To overcome this problem, a temperature probe can be positioned close to the FBG, allowing a post analysis data correction.

In the framework of the MEDiterranean-SUpersite Volcanoes (MED-SUV) project, we developed and tested a three-axial strain sensor attaining submicrostrain resolution on the vertical axis and microstrain resolution relative to the axes on the horizontal plane in static measurement.

II. PRINCIPLE OF OPERATION

The basic strain sensor elements are shown in Fig. 1. The vertical sensor is longer than those lying in the horizontal plane to get more sensitivity along this axis. The other sensors are shorter to keep the final cylindrical probe around a diameter of 10 cm, thus allowing an easy deployment into the bore-hole. The three sensors are placed along orthogonal axes [Fig. 1(a)] forming a Cartesian set. Each of them consists of a steel pipe containing a short length of silica fiber with an engraved FBG. One end of the pipe supports the fiber cable output, while the other end embeds the bare fiber tip by means a hard-type glue cap. The fiber is prestrained of some hundreds of microstrains to be sensitive to length changes. The volume inside the pipes is filled with a special two-component resin to prevent fiber damage and to keep it mechanically stable. Two steel disks applied on each pipe provide a good grip between the device and the external environment [Fig. 1(b)].[11,12] A Pt100 temperature probe is positioned along the vertical axis allowing thermal monitoring of the whole device. A polyvinyl chloride (PVC) pipe mold is used during fluid grout pouring, forming in this way a pillar of 370×96 mm^2 (length × diameter). This grout has been chosen because its Young modulus after hardening is similar to that of basalt.[13] The final sensor after grout drying and PVC tube removal is shown in Fig. 1(c), together with the optical fiber cables and the Pt100 cable.

This device, with just two sensors in the horizontal plane, can only measure two of the three components of the horizontal strain, and the vertical probe is inherently more sensitive being the longest. These choices have been dictated by ease of assembly and by the prototype nature of the instrument which is intended to explore some basic features in view of future developments. As we will see in the following, the lack of the third horizontal sensor is not a real limitation for the reconstruction of the signals because of the attention we posed in the alignment of the probe along the cardinal axes during its deployment.
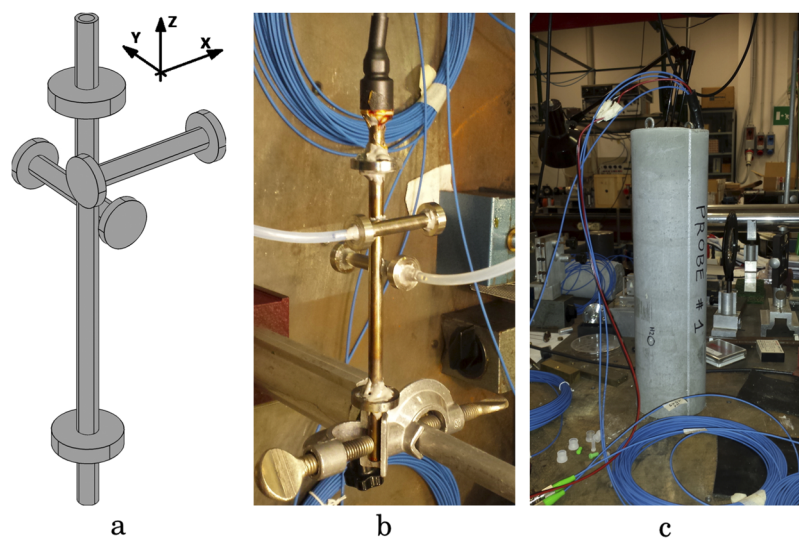

a b c

FIG. 1. The three-axes probe. (a) Scheme of the sensors, (b) the assembled sensors, and (c) the final probe.

The schematic in Fig. 2 shows the optical and electrical setup. The interrogation and the read-out system are composed by a continuous 10 mW Super-Luminescent emitting Diode (SLD), an in-fiber light circulator, a 1 × 3 optical coupler, an Arrayed Waveguide Grating (AWG), six Photo-Diodes (PDs), and an Analog to Digital Converter (ADC) device called GILDA (Geophysical Instrument for Low power Data Acquisition)[14] developed by the section of Napoli of the Istituto Nazionale di Geofisica e Vulcanologia (INGV). The broadband radiation from the SLD is sent to each sensor through the coupler, and the light reflected by the relative FBG is directed to the AWG by means of the circulator. The AWG is a passive optical device with equally spaced transmission windows, each centered at a predefined wavelength. Our AWG has 16 optical transmission channels (just six of them are really used) in a spectral grid according to the standard International Telecommunication Union ITU-T G.694.1.[15] Each channel has a −3 dB bandwidth of 50 GHz and a relative separation of 100 GHz (respectively, 0.4 nm and 0.8 nm at 1550 nm). The AWG device is temperature controlled to within a hundredth of a degree Celsius in a day to assure spectral stability to the optical channel power transmission. Six transimpedance amplified photodiodes receive the light signals from the appropriate AWG channels and transmit them to the GILDA datalogger. The signals of the borehole and AWG temperature probes are acquired as well. The Bragg wavelength variations coming from each sensor are analyzed following the principle of the paper of Su and Huang.[16] Using their notation, $P(k)$ and $P(k + 1)$ are the optical powers transmitted by the (k) and $(k + 1)$ adjacent AWG channels,

$$P(k) = (1 - L) \int L(\lambda) I_s(\lambda) R_{FBG}(\lambda, \lambda_b) T_{AWG}(k, \lambda) d\lambda, \quad (4)$$

$$P(k + 1) = (1 - L) \int L(\lambda) I_s(\lambda) R_{FBG}(\lambda, \lambda_b) T_{AWG}(k + 1, \lambda) d\lambda. \quad (5)$$

These quantities are the function of λ_b and are detected by the photodiodes of the respective channels. L is the optical attenuation of the whole system, $I_s(\lambda)$ is the intensity of the light source, $R_{FBG}(\lambda, \lambda_b)$ is the reflection spectrum from a FBG which is described by an analytical function,[10] and $T_{AWG}(k, \lambda)$ is the normalized transmission function of an AWG channel that can be approximated by a super-Gaussian of the kind $\exp\left(-(\lambda - \lambda_b)^4/\sigma^4\right)$. The product $I_s(\lambda) R_{FBG}(\lambda, \lambda_b) T_{AWG}(k, \lambda)$ has a small value when λ is far away from λ_b and $I_s(\lambda)$ can be consider as a constant in a narrow range of wavelength around λ_b. Therefore, defining the power ratio S as

$$S(\lambda_b) = \frac{P(k + 1) - P(k)}{P(k + 1) + P(k)}, \quad (6)$$

we get the simplified form

$$S(\lambda_b) = \frac{\int R_{FBG}(\lambda, \lambda_b) T_{AWG}(k + 1, \lambda) d\lambda - \int R_{FBG}(\lambda, \lambda_b) T_{AWG}(k, \lambda) d\lambda}{\int R_{FBG}(\lambda, \lambda_b) T_{AWG}(k + 1, \lambda) d\lambda + \int R_{FBG}(\lambda, \lambda_b) T_{AWG}(k, \lambda) d\lambda}. \quad (7)$$

The reading of the intensity of two adjacent AWG channels is used to recover the Bragg wavelength shift through Eq. (7) ("S-ratio algorithm").

When the Bragg wavelength λ_b shifts because of a strain (or temperature) perturbation, the S-ratio value changes in the same direction remaining between the value of −1 (λ_b at the center of the lower wavelength AWG channel) and +1 (λ_b at the center of the higher wavelength AWG channel). The best sensitivity and widest dynamic range are obtained when λ_b is initially at midway between the channel k and the channel $(k + 1)$ of the AWG (Fig. 3). We characterized the wavelength interrogation system through laboratory tests that indicated a dynamic range of more than 700 pm and a resolution better than 0.05 pm for the most performing sensor (the vertical one).

Calibration tests have been extensively conducted during laboratory runs, both on individual steel frame FBG sensors and on the final three-axes device. We changed the temperature of the sensor and used a high-resolution wavelength meter to record the Bragg wavelength variations. In this way, it has been possible to obtain an experimental point-to-point relation between $\Delta\lambda_b$ and ΔS, obtaining the responsivity curve λ_b vs S. This relation has been fitted obtaining the Bragg wavelength vs S-ratio calibration curve (Fig. 4). It is not possible to fit the experimental data in the whole S range (−1, +1) with a single function, so we used a linear relation for S between −0.6 and 0.6 and a more complicate function for $0.6 < |S| < 1$,
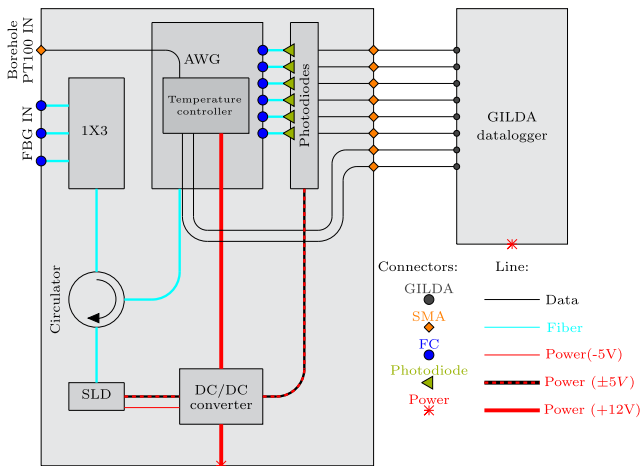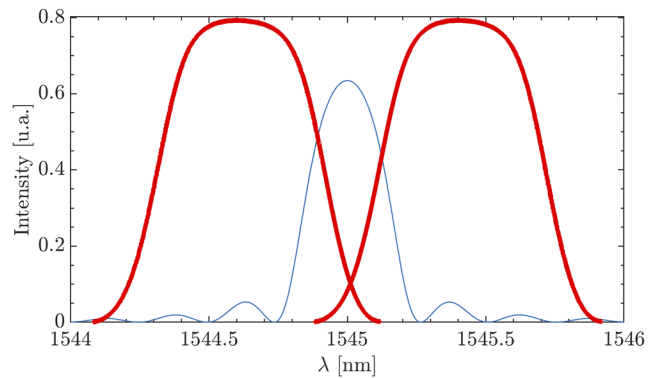

FIG. 2. Opto-electronic setup.

FIG. 3. Transmission of two consecutive AWG channels (red) and reflectivity of a FBG having its λ_b at midway between those windows (blue).
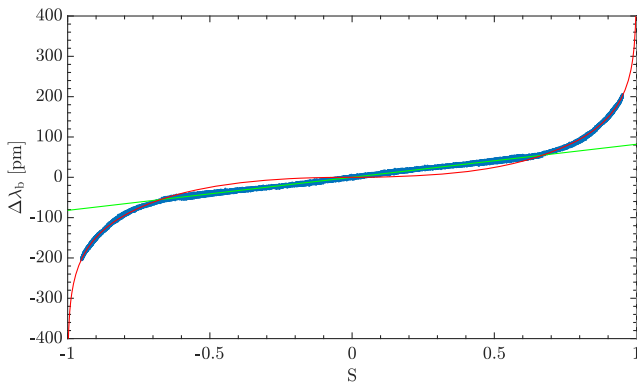
FIG. 4. Wavelength variation vs *S-ratio*. The blue dots are the data, the green line is the linear fit, and the red curve is the arctanhlike fit.

$$\Delta\lambda \text{ (pm)} = 82S \quad -0.6 \leq S \leq 0.6, \quad (8)$$

$$\Delta\lambda \text{ (pm)} = 113.07S|S|^{0.27}\text{arctanh}(|S|)^{1.06} \quad 0.6 < |S| < 1. \quad (9)$$

Equation (9) is the result of a heuristic choice starting from the general form $AS^b \text{arctanh}(S)^c$ and considering just S positive values (the extension to S negative values has been implemented by applying the absolute value $|S|$).

For the three strain probes, after their embedding into the grout pillar, we had approximately starting S values of −0.3, 0.7, and 0.95 for Vertical (V), East-West (EW), and North-South (NS), respectively (this notation will be clearer in the following when referred to the geographic axes). The NS probe is found to feature a lower sensitivity; indeed, the fit function Eq. (9) is less accurate for $|S|$ approaching 1. Despite the attention we paid during the development of the device, the final wavelength of the embedded sensors is not fully predictable because the Bragg grating was subjected to various stresses caused both by the curing of the resin used for their initial casing into the steel tubes and the final grout sealing. In view of a next generation device, the most practical solution to warrant an overall good sensitivity could be to employ an AWG with a channel spacing of 50 GHz (even if at the expenses of a reduced dynamic range) and with Gaussian shaped channels. This last option would allow a better resolution on individuating the center of each AWG channel with consequent less incertitude in recovering $\Delta\lambda_b$ with $|S|$ approaching 1. The adoption of thermally tunable AWG to match at the best the Bragg wavelengths could be a solution as well.

Once completed, the prototype was tested against calibrated compressions through a Universal Testing Machine (UTM). We obtained the relation between wavelength and strain in picometer (pm) vs $\mu\varepsilon$. This last calibration confirmed what is already known from the literature,[17,18] validating the approximate correspondence $\Delta\lambda_b = 1 \text{ pm} \rightarrow \Delta\varepsilon = 1 \mu\varepsilon$. Note that the AWG module is sensitive to thermal variations with a shift of the central wavelengths of its channels of about 1 pm/°C. To avoid signal fluctuations, this device has been actively regulated to a temperature of about 32 °C with this temperature kept stable within 0.01 °C over one day. The electrical power consumption of the whole system (SLD thermal and current control, photodiodes amplification, AWG thermostatation, and GILDA ADC) is of the order of 10 W. Therefore, the unit can be

powered although the solar panels are connected to trickle-charged batteries.

The wavelength interrogation technique we adopted provides a low-cost, compact, and high-performance solution for FBG sensors, while most of the more common read-out systems (tunable Fabry-Perot filters, Mach-Zender interferometers, optical grating devices, and so on) make use of expensive and delicate components.

III. SENSOR INSTALLATION

The installation site is Serra La Nave (SLN) Ragalna, Catania 37.69340° N, 14.97420° E, elevation 1740 m, in the facilities of the Astrophysical Observatory managed by INAF (Istituto Nazionale di Astrofisica). Figure 5 shows the location of the seismic/Global Positioning System (GPS) station indicated with the acronym ESLN (codename of the seismic/GPS station located in Serra La Nave, Ragalna, Catania, Italy, see Fig. 5), a few tens of meters away from the installation site of the FBG sensor. Other stations belonging to the Istituto Nazionale di Geofisica e Vulcanologia-Osservatorio Etneo (INGV-OE) permanent network[19] are shown in Fig. 5. All these stations are equipped with a Trillium-40s three component seismometer. Moreover, the Monte Denza (MDZ) bore-hole (−28 m) tilt station[20] is also indicated.

A 8.5 m deep and 15 cm wide borehole was drilled, and a first layer of about 20 cm of grout was poured into. Afterward, the cement pillar containing the sensors was lowered and rested on this fluid substrate. Soon after, the sensor was covered by a second grout casting up to filling a column height of about 1 m. Unfortunately, it was not possible to install the sensor at greater depth to ensure a higher thermal stability and to minimize the thermo-elastic ground displacement.[21] Indeed, when the depth of about 8.5 m was reached, we found a mass of fractured rock and we had to stop drilling. The casing grout is the same of that constituting the sensor pillar.
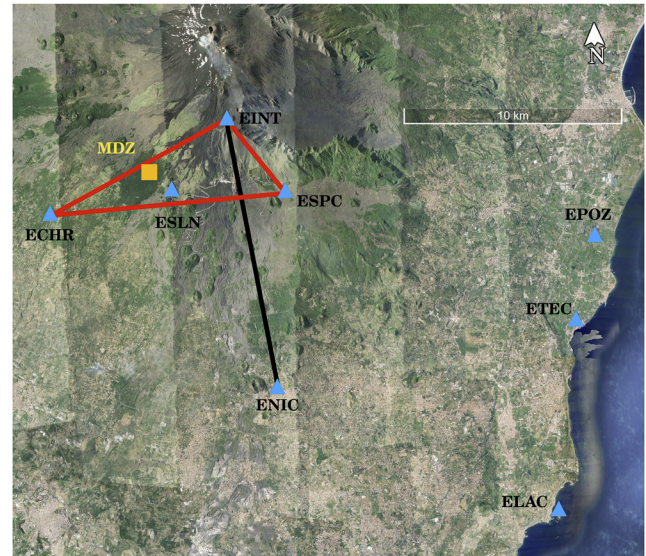

FIG. 5. Seismic/GPS (blue filled triangle) and tilt (yellow filled square MDZ) stations map. Black and red lines connect stations considered for calculation in Secs. IV A and IV B.

It has a low volume variation during its curing and has a Young modulus of about 27 GPa, close to the basalt value. In this way, the stress field is efficiently transferred to the device in the borehole. The optical and electrical (for the Pt100 probe) cables are protected by a PVC pipe running from the bottom of the borehole to the opto-electronic control box situated about 10 m far from the borehole itself. The pillar was positioned to orient the horizontal sensors along the north-south and east-west axes. The positioning angular error was estimated to be within a few degrees, and in the following, we will refer to NS (North-South) and EW (East-West) sensors. V (Vertical) is the vertical sensor. The electro-optical read-out system and the GILDA acquisition system are housed into the control box, which is a thermally insulated container $70 \times 50 \times 50$ cm^3 provided with specific feedthroughs for cable connections and power supply. This box is compliant with United States military standards MIL-STD-810,[22] and it is suitable to sustain high thermal excursions, rain, and snow. The system's power comes from the observatory. The GILDA data acquisition system has 8 input channels: 6 photo-diodes (corresponding to the six AWG operative optical channels), a downhole temperature probe, and an internal box temperature probe. The sampling rate is 40 Hz at 24 bits, and a Wi-Fi bridge transfers the data to an indoor storage system in the facilities of the INAF observatory.

IV. DATA ANALYSIS AND RESULTS

After the installation of the FBG device, at the beginning of April 2016, a period of several months was necessary to allow the

curing of the filling grout. During this time, we monitored the data stream to verify its self-consistency and we tested the reliability of the data acquisition and transmission systems. We verified that the downhole temperature was quite stable, with small daily variations around an average of 8.7 °C. Besides, between April and July 2017, we had various technical problems and the system was off for a total of about 45 days.

Figure 6 shows the time series of the three strain components, air temperature, and rainfall between May 1, 2016 and September 1, 2018 (raw data averaged to one point every 30 min and fitting curves). A phase lag is visible between V and EW components. This lag is reduced passing from the second to the third annual cycle and probably will disappear a couple of years later. There is not a clear explanation for that, but we presume this is an effect due to some long term rock/grout settlement. We observe a better resolution on vertical and east-west sensors because the Bragg wavelength of the north-south sensor falls almost in the middle of an AWG channel, implying that the *S-ratio* algorithm has a poorer sensitivity in recovering the wavelength variations. Figure 7 shows the power spectral density (PSD) of the V and EW components. Signals at one day (about 10^{-5} Hz) and its harmonics components are visible due to the daily thermo-elastic effect, while the origin of the peak at about 0.05 Hz (20 s) is unknown.

A. Data fitting

As known from the literature,[8,23] especially in the first months following the installation of a borehole strainmeter, two distinct
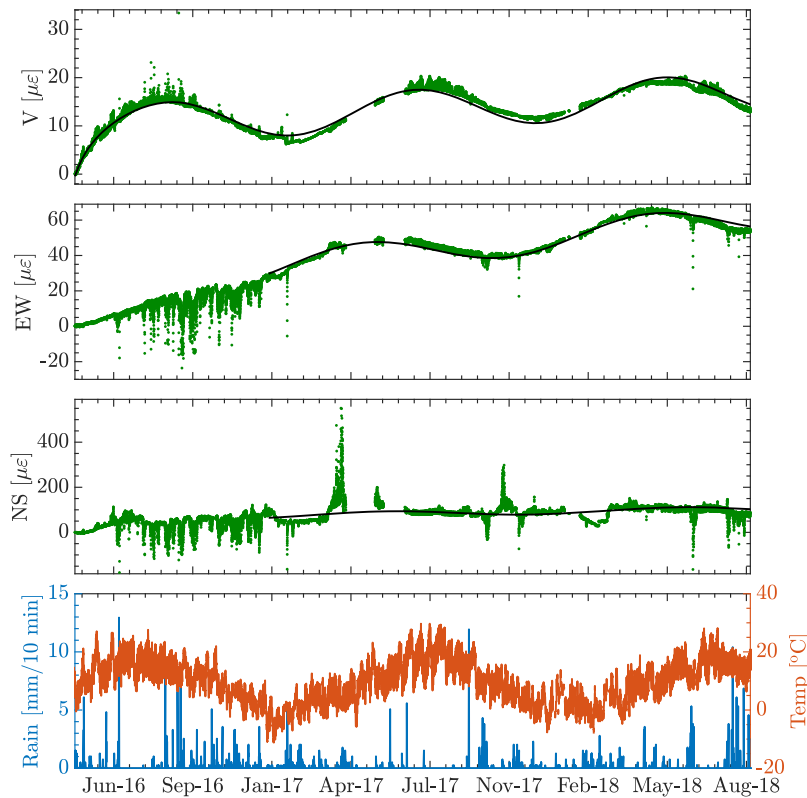

FIG. 6. From to to bottom: Vertical (V), East-West (EW), and North-South (NS) raw strain data (green) with their fit functions (black); air temperature (red) and rainfall data (blue) recorded by the Serra La Nave meteo station. Note the different scale for the NS component.
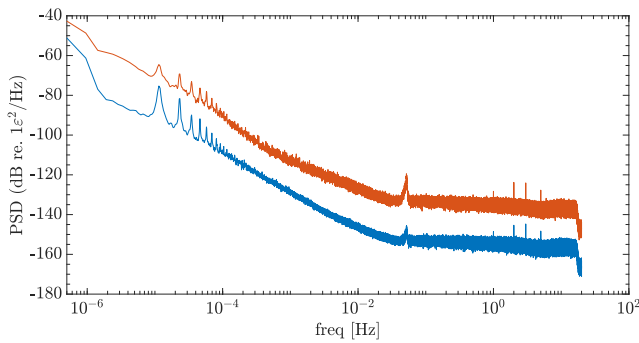
FIG. 7. Power Spectral Density (PSD) of east-west (orange) and vertical (blue) strain sensors.

phenomena must be considered: the tendency of the well to close again due to the natural resettlement of the rock, and the solidification of the contact cement between the strainmeter and the walls of the well itself. The first effect causes a contraction of the volume of the instrument, while the second one can induce both contraction and dilatation depending on the type of grout in relation to Young's modulus of the rock. Basically, an exponential or polynomial fit of the raw data can be used to simultaneously account for both effects. In our case, an exponential fit is suitable for the vertical sensor V. Moreover, we must consider the effect of the annual thermo-elastic behavior, which can be modeled simply as a sine wave. The period of this sine wave results to be about 313 days. In the complete expression of the fit, there is also a linear part that accounts for the "long term" trend.

The general expression of the fit function for the vertical sensor data is

$$y_0 + a(t - t_0) + Be^{-\frac{t-t_0}{\tau}} + K\sin(w(t - t_0) + \phi), \quad (10)$$

where y_0 is a constant, a is the long-term "epochal" trend, B is the "well-cement" coefficient, t_0 is the time of installation (April 8, 2016), τ is the time-constant characteristic of the well-cement process, K is the coefficient of the thermo-elastic behavior, $w = 2\pi/T$

with T being the period, and finally ϕ is the phase. We observe that the most significant quantity is a because it expresses the strain trend over the long term.

Note that the structure of V vs time is similar to the behavior shown in Fig. 8 of DeWolf et al.,[24] where a deep borehole vertical optical fiber strainmeter is described. No spikes removing procedure has been attempted before raw data fitting.

For the V probe, we obtain $a = 3.50 \pm 0.3$ $\mu\varepsilon$/yr. In the case of the EW sensor, the global fitting procedure does not give fully satisfactory results and, with a conservative choice, we decided to start the calculation from January 1, 2017 using just a linear plus a sinusoidal function. In this way, we get a trend of 15.9 ± 2.1 $\mu\varepsilon$/yr. For the poor-quality NS data, we adopted the same fitting procedure, obtaining a trend of 21.4 ± 7.9 $\mu\varepsilon$/yr. The reported errors represent the a parameter fit variability within a 99% confidence interval for a normal distribution of the fit residuals and using a least-square recursive algorithm. For the V component, the fit estimations for the parameters B, τ, and K give values of about 28 microstrain, 18 days, and 4.1 microstrain, respectively. We can consider negligible the exponential contribution to Eq. (10) after a time period equal to 5τ that is 3 months. This is consistent with the expected borehole grout curing time. The annual thermo-elastic amplitude values K for V, EW, and NS (about 4.1, 8.7, and 12 $\mu\varepsilon$, respectively) are in a good agreement with the model proposed in Ref. 25, postulating 1000 m for the characteristic traveling thermal wavelength of the surface temperature variation. The diurnal (day/night) thermo-elastic effect from the surrounding rocks is well visible on the data from the three sensors (Fig. 8). The average amplitude of this effect for V (0.1–0.2 $\mu\varepsilon$) and EW (1 $\mu\varepsilon$) is consistent with the cited model. Concerning the NS sensor, the diurnal amplitude results to be about 5 $\mu\varepsilon$, larger than the predicted value. However, the model does not take into account possible differences in the effect along different horizontal directions. In a real situation, topography and soil peculiarities can make the difference. The daily thermo-elastic effect is larger by about two orders of magnitude than the typical amplitude of the solid Earth tides that can not be thus observed.

Comparing air and borehole temperature data, we observe a phase lag of about 162 days, that is, summer/winter seasonal variations are almost inverted in the borehole, where the
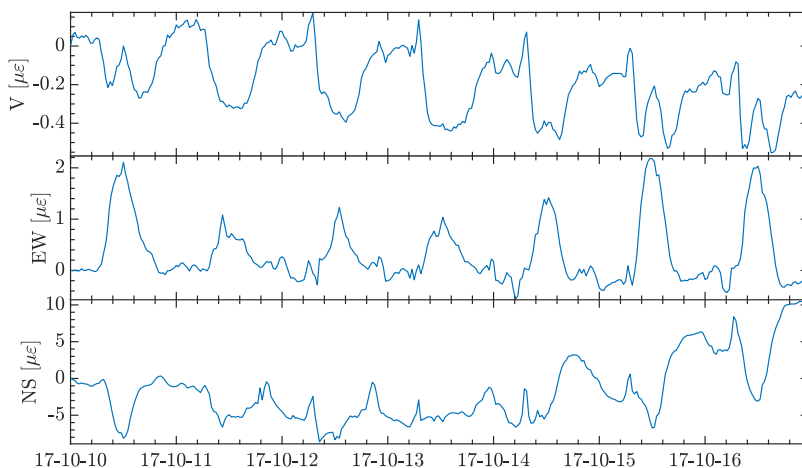

FIG. 8. From up to bottom: V, EW, and NS daily thermo-elastic strain.

temperature average value is 8.73 °C with yearly fluctuations of 0.22 °C as expected.[26] The borehole temperature is essential to the first and fundamental data reduction.

In fact, fiber optic strain sensors are sensitive to temperature variation,[10] and this effect must be subtracted from the raw data to obtain the signal induced by strain. To do this, we obtained in a laboratory experimental run the wavelength/temperature coefficients of the sensors (about 25 pm/°C) and the original strain data are in this way corrected.

Heavy rain episodes can have a great influence on a shallow deployed instrument. The effect is especially evident on EW and NS components, while the V component is affected to a minor extent. The presence of spike signals is related to rainfall (Fig. 6), and we can observe that spikes rate is higher during the first 6/8 months following the installation. That is probably because a quite long settlement time has been needed.

Spikes are of greater amplitude on EW and (especially) NS components. It is our opinion that the cylindrical symmetry of the borehole (vertical vs radial directions) plays a role for that. Indeed, following rainfall episodes, there is a direct radial compression of the borehole as it is proven by the compressional aspect of the EW and NS spikes. In correspondence, V spikes are predominantly upward and of smaller amplitude. This is qualitatively in accordance with the elastic model predicted by Eq. (28). Just three or four cases over 28 months seem to constitute an exception for this "rule," but an explanation is not simple for that. The difference in spikes amplitude between EW and NS may be also due to strong inhomogeneities in the transmission of meteoric water occurring along different directions over the horizontal plane.

To complete our analysis, we must move from the data that represent the relative length variation of the single sensor (that is the acquired raw data) to the effective strain along the main directions in the horizontal plane, i.e., east-west and north-south.[27-30]

Since in our case we have only two horizontal sensors, it is only possible to compute areal dilatation and one component of shear strain. Note that our choice not to provide the third horizontal sensor has been done to simplify the setup and the read-out (moreover one more ADC card was not available at the time of the sensor positioning). However, our main goal is to test the sensitivity of the prototype and to learn what improvements could be done on a second-generation device.

B. Principal axes strain calculation

For each horizontal i sensor, we can write the linear strain e_i,[30]

$$e_i = C\varepsilon_A + D\gamma_1 \cos(2\phi_i) + D\gamma_2 \sin(2\phi_i), \quad (11)$$

$$\varepsilon_A = \varepsilon_E + \varepsilon_N, \quad (12)$$

$$\gamma_1 = \varepsilon_E - \varepsilon_N, \quad (13)$$

$$\gamma_2 = 2\varepsilon_{EN}. \quad (14)$$

Indicating $e_1 = \varepsilon_{EW}$ and $e_2 = \varepsilon_{NS}$, we get

$$\varepsilon_E + \varepsilon_N = \frac{1}{2C}(\varepsilon_{EW} + \varepsilon_{NS}), \quad (15)$$

$$\varepsilon_E - \varepsilon_N = \frac{1}{2D}(\varepsilon_{EW} - \varepsilon_{NS}), \quad (16)$$

where ε_E and ε_N are, respectively, the east-west and the north-south principal horizontal strains and γ_2 is the engineering shear strain. ε_A and γ_1 are the definitions of areal and differential strain. ϕ_i is the angle between the strain gauge i and the east-west direction, measured counterclockwise. Because of the attention we dedicated in orientating the axes of the pillar probe, we can pose $\phi_1 \simeq 0$ and $\phi_2 \simeq \pi/2$. The C and D coefficients represent the areal and the shear coupling factors. As a first approximation, the theory of elasticity for an isotropic medium indicates C = 3 and D = 6.[30] We easily obtain

$$e_1 \equiv \varepsilon_{EW} = 3\varepsilon_A + 6\gamma_1, \quad (17)$$

$$e_2 \equiv \varepsilon_{NS} = 3\varepsilon_A - 6\gamma_1, \quad (18)$$

$$\varepsilon_E = \frac{1}{4}\left[\frac{1}{3}(e_1 + e_2) + \frac{1}{6}(e_1 - e_2)\right], \quad (19)$$

$$\varepsilon_N = \frac{1}{4}\left[\frac{1}{3}(e_1 + e_2) - \frac{1}{6}(e_1 - e_2)\right]. \quad (20)$$

Because of the poor quality of NS data (and consequently of their fit), it is not realistic to utilize the above results to get the whole time series for ε_E and ε_N. It makes more sense to consider EW and NS evolution over short periods or to look at the linear part of their annual trends. To validate this approach and to test the sensor calibration, we considered the M 6.5 seismic event which occurred in central Italy on October 30, 2016, at a distance of about 600 km.[31] The P-wave arrival time at Serra La Nave is 06:41:38 as confirmed by the signal from the ESLN seismometer. In Fig. 9, the data from the individual sensors are shown, averaged to 1 point each 100 s from their original sampling rate of 40 Hz. Seismic-induced slow transients are well observable for each component. Note the high and narrow peak on the V component at about 07:23. In correspondence of the event, the uncorrected displacements are

$$\varepsilon_V = 7.9 \ \mu\varepsilon, \quad (21)$$

$$e_1 \equiv \varepsilon_{EW} = -31.6 \ \mu\varepsilon, \quad (22)$$

$$e_2 \equiv \varepsilon_{NS} = -89.6 \ \mu\varepsilon. \quad (23)$$

After the reduction in the principal axes, we get

$$\varepsilon_A = \varepsilon_E + \varepsilon_N = -20.2 \ \mu\varepsilon, \quad (24)$$

$$\gamma_l = \varepsilon_E - \varepsilon_N = 4.8 \ \mu\varepsilon, \quad (25)$$

and finally, we obtain

$$\varepsilon_E = -7.7 \ \mu\varepsilon, \quad (26)$$

$$\varepsilon_N = -12.5 \ \mu\varepsilon. \quad (27)$$

We can write[32]

$$\varepsilon_V = -\frac{\nu}{1 - \nu}\varepsilon_A, \quad (28)$$

where $\nu \approx 0.25$–0.3 is Poisson's coefficient for basaltic rock. With this formula, we find a calculated value (ε_V calc) $\approx 7.7 \ \mu\varepsilon$ which is in a very good agreement with the measured one Eq. (21). This exercise confirms also the autoconsistency of the data. Values in Eqs. (21),
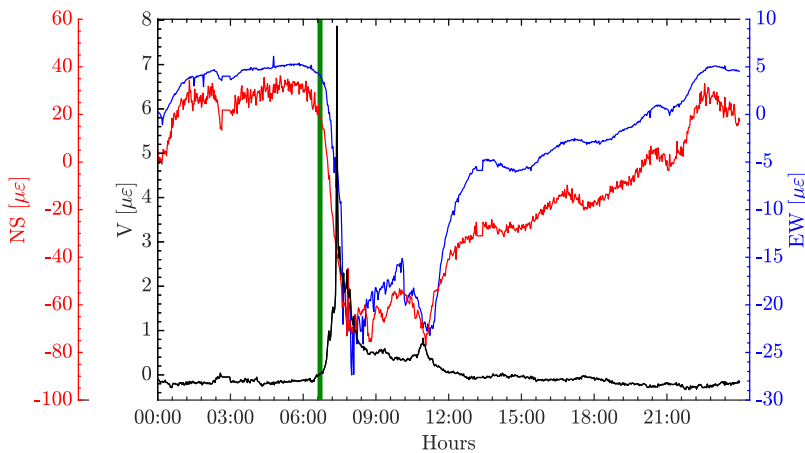
FIG. 9. October 30, 2016 Central Italy Earthquake co-seismic dislocation. North-south (red), vertical (black), and east-west (blue). The vertical green line identifies the P-wave arrival time.

(26), and (27) are much higher than the value of about 0.3 nanostrain predicted in the case of a co-seismic displacement by the elastic dislocation model for a M6.5 earthquake with an epicentral distance of 600 km.[33] The paper of Barbour *et al.*[34] shows that co-seismic observed strain may exceed by an order of magnitude the calculated one, but that does not explain the anomalous values we recorded.

We postulate that the huge discrepancy between theory and observation might be due to the peculiarity of our installation site, placed on the slope of an active volcano. It is possible that distant earthquakes may induce volcanic phenomena as tremor variations, lava fountains, local seismic sequences, and even eruptions.[35] Perhaps, in certain situations, regional earthquakes of relevant magnitude might drive also elastic displacement and strain episodes.

In the whole period 2016/05/01 up to 2018/09/01, we get the following trends:

$$\dot{\varepsilon}_V = 3.5 \pm 0.3 \ \mu\varepsilon/\text{yr}, \tag{29}$$

$$\dot{\varepsilon}_E = 2.9 \pm 0.6 \ \mu\varepsilon/\text{yr}, \tag{30}$$

$$\dot{\varepsilon}_N = 3.3 \pm 1.1 \ \mu\varepsilon/\text{yr}. \tag{31}$$

These values are the result of fitting the data, taking the respective linear coefficients *a* [Eq. (10)] and reducing these quantities

to the principal axes. Error values shown in Eqs. (30) and (31) represent the result of the error propagation starting from the fitting "*a*" parameters and following equations (19) and (20).

These values can be compared with data from GPS stations, following the methods described in Secs. IV C and IV D.

C. Strain reconstruction via pairs of GPS stations

The time series from the Etna GPS database are considered for two pairs of GPS stations located relative to SLN approximately along east-west [ECHR and ESPC (codenames of the seismic/GPS station located near ESLN)] and along north-south [EINT and ENIC (codenames of the seismic/GPS station located near ESLN)] (Fig. 5). For each couple of stations, the relative displacement is considered, and the strain along each axis is obtained by dividing the relative displacement for the distance between the stations (Fig. 10).

In this way, we obtain the following estimates:

1. East-west direction

During the period September 2016 to September 2018, ECHR moves toward west by 16.9 mm/yr, while ESPC toward east by 9.5 mm/yr, in total 26.4 mm/yr over a distance of about 10.1 km. We get an expanding trend of 2.6 $\mu\varepsilon$/yr. Considering all the
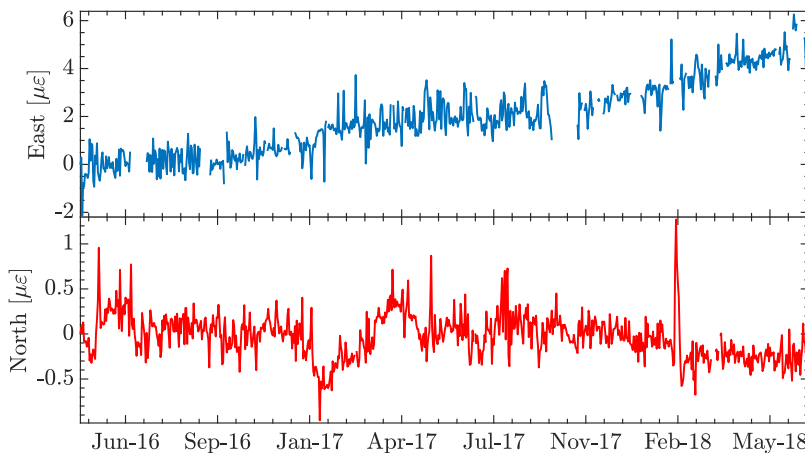

FIG. 10. Reconstructed strain from GPS stations data ECHR-ESPC (blue) and ENIC-EINT (red).

approximations, this value is in a very good agreement with our measurement of ε_E.

2. North-south direction

Both EINT and ENIC move toward south at a rate of 14.3 and 12.3 mm/yr, respectively. This different rate results in a net contraction along the line of about $-0.17~\mu\varepsilon$/yr, considering the station-to-station distance of 11.9 km.

This results does not match our experimental value $\dot{\varepsilon}_N$. However, strain information recovered from GPS stations data gives values averaged over the distance between the stations themselves, that is, some kilometers. Our instrument is subjected both to massive and to local point source ground displacements. In this sense, it is not surprising a partial disagreement with other strain estimation techniques based on the hypothesis of ground homogeneity on some square kilometers.

3. Vertical direction

As mentioned, our device measures a vertical trend $\dot{\varepsilon}_V = 3.5~\mu\varepsilon$/yr. Starting from the mean annual vertical velocities of the three nearest GPS stations (ECHR, EINT, ESPC), it is possible to calculate the algebraic average of the variations with respect to SLN. We thus obtain a trend of 6.5 mm/yr for the rise-up of the SLN site. Data from the three closest GPS stations positioned at the sea level over the coast line [Fig. 5 EPOZ, ETEC, and ELAC (codenames of the closest seismic/GPS station to ESLN at the sea level over the coast line) from north to south], show in the same period an average trend of about −2 mm/yr. So, we can make the hypothesis of a vertical deformation involving a height of about 1.74 km (SLN elevation) with a net trend of [6.5 − (−2)] = 8.5 mm/yr, corresponding to 4.9 $\mu\varepsilon$/yr. This estimation, even if quite raw, accounts for the order of magnitude and agrees substantially with our instrumental value.

D. Strain reconstruction via UNAVCO applet

We use the algorithm provided by UNAVCO (University NAVstar COnsortium, a nonprofit university-governed consortium that facilitates geoscience research, and education using geodesy, www.unavco.org).[36]

This algorithm provides $\varepsilon_{XX} = \varepsilon_E$ and $\varepsilon_{YY} = \varepsilon_N$ (and also ε_{XY}). These values represent averages within a triangle having as vertices three GPS stations whose displacement velocities in millimeter per year are known. Using data from ECHR, EINT, and ESPC stations (SLN falls within the triangle about 800 m south-west from its centroid, as shown in Fig. 5), we get on east-west a strain trend of 2.5 $\mu\varepsilon$/yr and on north-south a strain trend of −0.4 $\mu\varepsilon$/yr. These values are in accordance with those obtained with the method based on GPS stations data.

While the EW strain velocity deduced from the two above methods (pairs of GPS stations and UNAVCO calculator) is in agreement with the results from the FBG sensor data, a remarkable difference is found along the NS direction. To address this inconsistency, we should also consider the effect of local tectonic structures (e.g., the Ragalna Faults System) on the strain data from the FBG sensor at SLN.[37–39] Nonetheless, it is worth noting that our measured areal strain rate $\dot{\varepsilon}_A = \dot{\varepsilon}_E + \dot{\varepsilon}_N = 6.2 \pm 1.3~\mu\varepsilon$/yr is in accordance with the value of about 7 $\mu\varepsilon$/yr that can be deduced from the data shown in Ref. 40.

V. SEISMIC EVENTS

A. Regional and local events

As an example of regional event, Fig. 11 shows the records of the V and EW channels during the already cited M 6.5 seismic event that occurred on October 30, 2016 with epicenter in central Italy. Each trace is compared with the corresponding seismic signal from the SLN seismometer. Strain data are pass-band filtered between 0.01 and 10 Hz. The recorded strain amplitude of the order of tens of nanostrains is in a very good agreement with the model suggested by Barbour and Crowell.[41] By using Eq. (5) therein, we get in this case about 80 $n\varepsilon$ for the expected strain amplitude. Furthermore, local seismic events where utilized to make estimates of the sensitivity of the three instrumental axes. In particular, we consider two earthquakes that occurred on July 18, 2018 M 3.4 and hypocenter at a depth of 7–8 km. The epicenter of both events was only a few kilometer from SLN. Figure 12 shows the measured strain for the vertical and the east-west axes, together with the corresponding seismic signals from ESLN station. If we focus on the vertical component during the surface wave arrival of the first event (21:20:38 UTC), we note that the signals from the FBG sensor and seismometer are out of phase (Fig. 13). This is due to the fact that the seismogram is a velocity and the strain is proportional to a displacement.
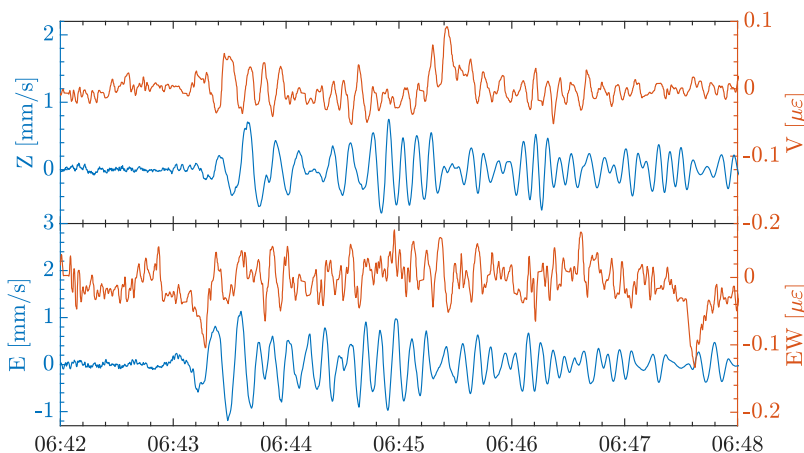

FIG. 11. Central Italy October 30, 2016 M6.5 Earthquake. From top to bottom: V strain (orange), vertical seismogram (blue), EW strain (orange), and EW seismogram (blue).
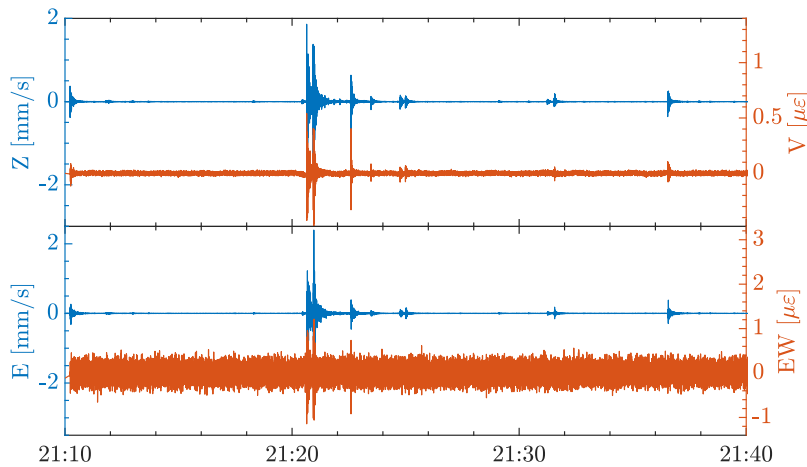
FIG. 12. July 18, 2018 Zafferana—Ragalna Earthquake. Top: vertical component of seismometer (blue) and strain (orange). Bottom: EW component of seismometer (blue) and strain (orange).

1. North-south sensor sensitivity

The north-south axis is blind to the events previously described, as well as to every event with amplitude below the order of several microstrain and occurring over a time scale shorter than a few tens of seconds. In this sense, the NS channel is scarcely suitable to observe seismic events, but it can evidence relatively small (even sub-$\mu\varepsilon$) medium to long term displacements occurring on time scales exceeding several minutes. However, strain changes occurring over time scales of months to years are difficult to be defined, even with deep borehole devices, due to the intrinsic difficulty in distinguishing them from instrumental artifacts.

B. Teleseismic events

Figure 14 shows the Mexico (M8.1 2017/09/08) teleseism recorded by the V (Vertical) strain sensor component of our instrument and by the corresponding component of the Serra La Nave (ESLN) seismometer. The strain signal is band-pass filtered between 0.016 and 0.15 Hz (6.7–60 s). In this frequency band, the resolution of V is better than 10 nε. We also recorded the teleseismic event of November 13, 2016 (M 7.8) in New Zealand: the strain signal is observable on the V and EW components. Figure 15 shows

the strain traces after pass-band filtering between 0.005 and 0.1 Hz (10–200 s) and the corresponding seismic signals from ESLN. It is possible to obtain an estimate of the strain expected on the horizontal plane by the parameters of the earthquake (magnitude and angular distance).[42,43] The relation proposed for the maximum strain (nanostrain units) is[42]

$$\log_{10}(\varepsilon) = 0.95M - 1.65 \log_{10}(\Delta) - 2.8, \qquad (32)$$

where M is the moment magnitude and Δ is the angular distance in degrees. This formula provides peak values, respectively, of the order of 43 nε for the Mexico event (distance 10 576 km, Δ = 95°, azimuth 76.8°) and of 9 nε for the New Zealand one (distance 18 079 km, Δ = 162°, azimuth 299.1°). Note that the formula is thought for radial and transverse components and we have a clear horizontal signature (EW) in the case of the New Zealand earthquake only. Moreover, the EW strain amplitude we recorded for the New Zealand event is greater than the predicted one.

Anyway, considering all the limitations of this comparison between calculated and experimental data (i.e., lack of signature on the NS component of our instrument), we can conclude that the scale calibration of our strain device is substantially correct.
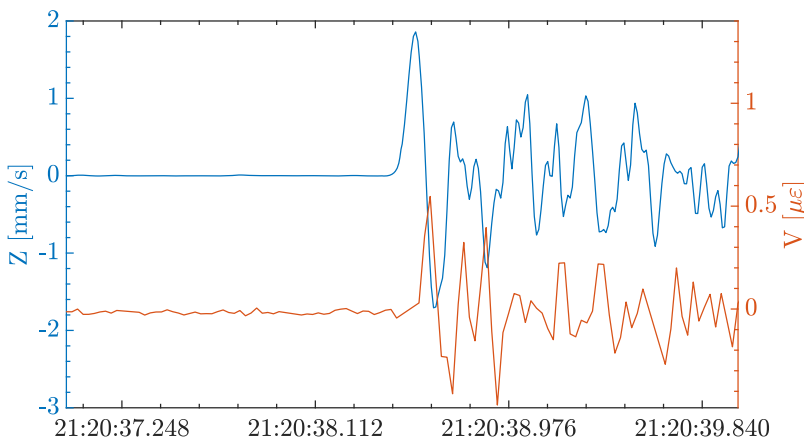

FIG. 13. Zoom of the M3.4 earthquake at 21:20:38 of July 18, 2018. From top to bottom: vertical component of seismometer (blue) and strain (orange).
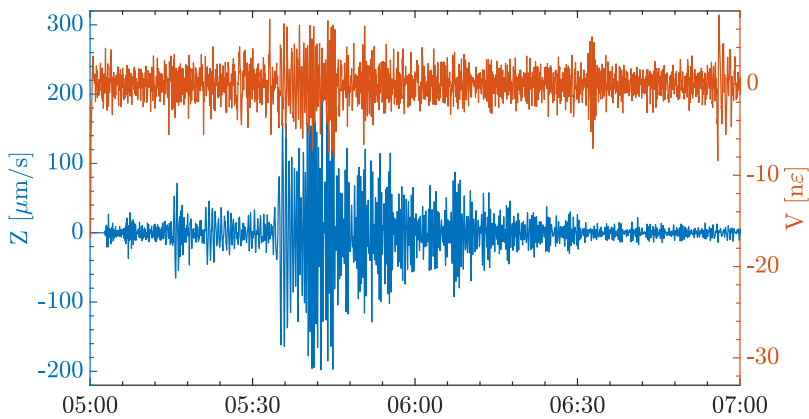
FIG. 14. September 8, 2017, Mexico M 8.1 teleseism. From top to bottom: vertical component of strain (orange) and seismic (blue) signal.
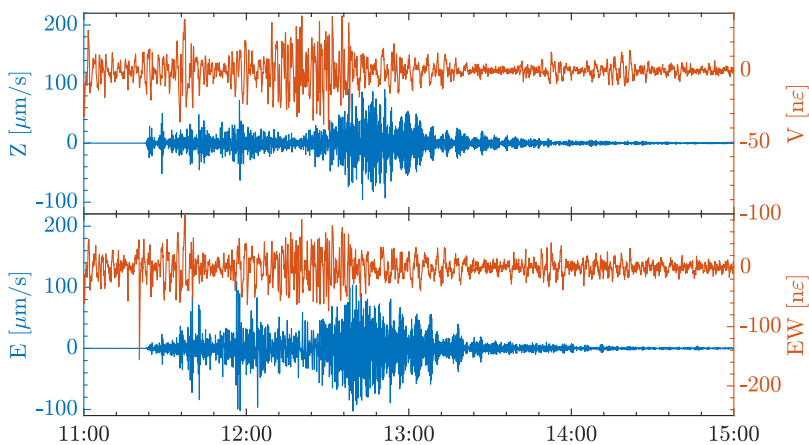

FIG. 15. November 13, 2016, New Zealand teleseism. From top to bottom: vertical component of strain (orange) and seismic (blue) signal, EW component of strain (orange), and seismic (blue) signal.

VI. ERUPTIVE EVENTS AND RELATIVE RAPID SLIP MARKS

At the beginning of 2017, an eruptive phase occurred from the southeast Crater Complex of Etna. This activity involved Strombolian explosions, ash emission, and emission of lava flows from different vents.[44] During this period, the most relevant feature in the signals from the FBG device is the sudden change ("step") in the average level of V and EW time series, that occurred between 8 and 9 February (Fig. 16). For both components, the amplitude of the change is about 0.4 $\mu\varepsilon$, while the sign is opposite (a decrease and an increase is observed in the signal from V and EW sensors, respectively). A similar change is not observed in the signal from the NS sensor. During almost the same interval, a change in the average level
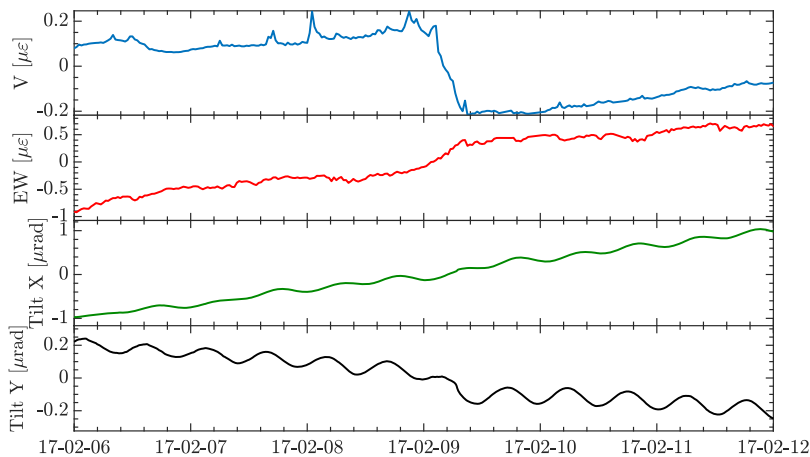

FIG. 16. The displacement event recorded on February 2017. From above: V strain (blue), EW strain (red), tilt X (green), and tilt Y (black).

of the signal was also observed in the data from the Monte Denza (MDZ) tilt station (Fig. 16), about 2 km from SLN (Fig. 5). The sudden change observed in both tilt and strain signals could reflect ground deformation associated with the ongoing eruptive activity. The shape of the signals shows the typical behavior induced by lava fountains and eruptions.[40] Strain and tilt amplitudes and duration are substantially in accordance with those of Ref. 45. In this work, the authors recorded strain and tilt signals originated by the same southeast Crater by means of instruments placed at a distance similar to that of our device. They recorded a volumetric strain ranging from 0.1 to 0.5 $\mu\varepsilon$ evolving in some hours. In that paper, a model for the event is also described, which is in accordance with the experimental data.

VII. CONCLUSIONS

We describe a three-axes FBG strain sensor for geophysical applications, with a dynamic range of hundreds of microstrains and submicrostrain resolution for its most performing axis. The sensor is suitable for borehole deployment, and the prototype described in the present paper has shown encouraging results. The performances of the device can be tailored to fit the requirements of volcano monitoring in harsh conditions, with special attention to the trade-off among resolution, ease of deployment, cost, and power consumption. Speaking of the cost, it is important to observe that our instrument has required a budget of a few thousands of Euro for the interrogation and the read-out unit. Including data acquisition and storage plus borehole drilling, the overall expense has been of the order of 15k Euro. This amount is one order of magnitude less than needed to install a conventional deep borehole strainmeter (Sacks-Everson[7] or Gladwin[46] type). As for the prototype device described here, the borehole is not deep enough to avoid the thermoelastic induced strain. Besides, some improvements must be done on the read-out technique to reach the best sensitivity for each sensor. A third and maybe a fourth sensor should be added in the horizontal plane to recover shear strain and for redundancy, even if their presence would complicate the whole probe geometry and its deployment. The architecture of our instrument turned out to be very reliable, with a duty cycle of about 95% over more than 2 years. This device could be intended as the basic element to get a detailed ground strain map over areas of some square kilometers. That could be realized by deploying an array of sensors in a star configuration with a single interrogation unit in the center and some individual boreholes at the vertices. Anyway, the experiment performed using this FBG strain prototype allowed us to gain a unique experience through which we will improve the performance of next-generation devices.

REFERENCES

[1] M. Majumder, T. K. Gangopadhyay, A. K. Chakraborty, K. Dasgupta, and D. K. Bhattacharya, Sens. Actuators, A **147**, 150 (2008).
[2] C. Campanella, A. Cuccovillo, C. Campanella, A. Yurt, and V. Passaro, Sensors **18**, 3115 (2018).
[3] P. Ferraro and G. De Natale, Opt. Lasers Eng. **37**, 115 (2002).
[4] T. Kogure and Y. Okuda, Geophys. Res. Lett. **45**, 4033, https://doi.org/10.1029/2018gl077607 (2018).
[5] Q. Liu, Z. He, and T. Tokunaga, Opt. Express **23**, A428 (2015).
[6] J. Chen, Q. Liu, and Z. He, J. Light. Technol. **35**, 4838 (2017).
[7] I. Selwyn Sacks, S. Suyehiro, D. W. Evertson, and Y. Yamagishi, Pap. Meteorol. Geophys. **22**, 195 (1971).
[8] A. Bonaccorso, A. Linde, G. Currenti, S. Sacks, and A. Sicali, J. Geophys. Res.: Solid Earth **121**, 4655, https://doi.org/10.1002/2016jb012914 (2016).
[9] K. Hill and G. Meltz, J. Light. Technol. **15**, 1263 (1997).
[10] A. Othonos, Rev. Sci. Instrum. **68**, 4309 (1997).
[11] G. F. Fernando, A. Hameed, D. Winter, J. Tetlow, J. Leng, R. Barnes, G. Mays, and G. Kister, Struct. Health Monit.: Int. J. **2**, 123 (2003).
[12] P. Biswas, S. Bandyopadhyay, K. Kesavan, S. Parivallal, B. A. Sundaram, K. Ravisankar, and K. Dasgupta, Sens. Actuators, A **157**, 77 (2010).
[13] See https://www.mapei.com/it/en/products-and-solutions/products/detail/mapegrout-hi-flow for MAPEI.
[14] M. Orazi and R. Peluso, Earth-Prints Solid Earth04.08, Volcanol, 2012.
[15] See https://www.itu.int/rec/T-REC-G.694.1-201202-I/en for ITU-T (2012).
[16] H. Su and X. G. Huang, Opt. Commun. **275**, 196 (2007).
[17] Z. Zhou, X. Zhao, W. Li Hong, and J. Ou, in *21st IMAC Conference and Exposition 2003 (IMAC XXI): A Conference and Exposition on Structural Dynamics* (SEM, 2003), pp. 1–10.
[18] I.-Y. Jang and Y.-W. Yun, Int. J. Concr. Struct. Mater. **3**, 33 (2009).
[19] S. Alparone, O. Cocina, S. Gambino, A. Mostaccio, S. Spampinato, T. Tuvè, and A. Ursino, J. Volcanol. Geotherm. Res. **251**, 16 (2013).
[20] S. Gambino, G. Falzone, A. Ferro, and G. Laudani, J. Volcanol. Geotherm. Res. **271**, 43 (2014).
[21] M. J. S. Johnston and A. T. Linde, Int. Geophys. **81**, 589 (2002).
[22] H. W. Egbert, J. IEST **48**, 147 (2005).
[23] E. A. Roeloffs and A. T. Linde, in *Volcano Deform* (Springer Berlin Heidelberg, Berlin, Heidelberg, 2007), pp. 305–322.
[24] S. DeWolf, F. K. Wyatt, M. A. Zumberge, and W. Hatfield, Rev. Sci. Instrum. **86**, 114502 (2015).
[25] J. Berger, J. Geophys. Res. **80**, 274, https://doi.org/10.1029/jb080i002p00274 (1975).
[26] T. Kusuda and P. R. Achenbach, ASHRAE Trans. **71**, 61 (1965).
[27] M. T. Gladwin and R. Hart, Pure Appl. Geophys. **123**, 59 (1985).
[28] R. H. G. Hart, M. T. Gladwin, R. L. Gwyther, D. C. Agnew, and F. K. Wyatt, J. Geophys. Res.: Solid Earth **101**, 25553, https://doi.org/10.1029/96jb02273 (1996).
[29] E. Roeloffs, *Introduction to Strain and Borehole Strainmeter Data* (unpublished), see https://www.unavco.org/education/professional-development/short-courses/2014/strainmeter/strainmeter.html.
[30] E. Roeloffs, J. Geophys. Res. **115**, B06405, https://doi.org/10.1029/2009jb006407 (2010).
[31] INGV—Istituto Nazionale di Geofisica e Vulcanologia, Boll. Sism. Ital. **07/2017**, 1–5 (2016).
[32] J. C. Harrison, J. Geophys. Res. **81**, 319, https://doi.org/10.1029/jb081i002p00319 (1976).
[33] F. K. Wyatt, J. Geophys. Res. **93**, 7923, https://doi.org/10.1029/jb093ib07p07923 (1988).
[34] A. J. Barbour, D. C. Agnew, and F. K. Wyatt, Bull. Seismol. Soc. Am. **105**, 431 (2015).

[35] A. Cannata, G. Di Grazia, P. Montalto, M. Aliotta, D. Patanè, and E. Boschi, J. Geophys. Res. **115**, B12304, https://doi.org/10.1029/2010jb007487 (2010).

[36] See http://www.science.earthjay.com/instruction/HSU/2016_spring/GEOL_460/GPS_geodesy for Excel Calculator: Strain within Triangle of GPS Sites (2016).

[37] G. Puglisi and A. Bonforte, J. Geophys. Res.: Solid Earth **109**, 1–15, https://doi.org/10.1029/2003JB002878 (2004).

[38] G. Barreca, A. Bonforte, and M. Neri, J. Volcanol. Geotherm. Res. **251**, 170 (2013).

[39] R. Azzaro, A. Bonforte, S. Branca, and F. Guglielmino, J. Volcanol. Geotherm. Res. **251**, 5 (2013).

[40] M. Aloisi, A. Bonaccorso, F. Cannavò, and G. M. Currenti, Front. Earth Sci. **6**, 109 (2018).

[41] A. J. Barbour and B. W. Crowell, Seismol. Res. Lett. **88**, 354 (2017).

[42] D. C. Agnew and F. K. Wyatt, Bull. Seismol. Soc. Am. **104**, 1846 (2014).

[43] J. Gomberg and D. Agnew, Bull. Seismol. Soc. Am. **86**, 212 (1996).

[44] INGV—Istituto Nazionale di Geofisica e Vulcanologia, Boll. Settim. **7**, 1–10 (2017).

[45] A. Bonaccorso, G. Currenti, A. Linde, and S. Sacks, Geophys. Res. Lett. **40**, 3579, https://doi.org/10.1002/grl.50692 (2013).

[46] M. T. Gladwin, Rev. Sci. Instrum. **55**, 2011 (1984).